WELDING RESEARCH

SUPPLEMENT TO THE *WELDING JOURNAL*, APRIL 2001
Sponsored by the American Welding Society and the Welding Research Council

Modeling Microstructure Development in Self-Shielded Flux Cored Arc Welds

Thermodynamic and kinetic models provide insight into microstructure evolution in self-shielded flux cored arc welds

BY S. S. BABU, S. A. DAVID, AND M. A. QUINTANA

ABSTRACT. Microstructure evolution in two self-shielded flux cored arc welds was investigated. Depending on the aluminum concentration, the two welds exhibited different microstructures. Welds with high aluminum concentration contained skeletal δ-ferrite microstructure. In contrast, welds with low aluminum concentration showed classic α-ferrite morphology. This difference in microstructure evolution is attributed to the relative stability of δ-ferrite and austenite during solidification and at high temperature after solidification. This microstructure development was successfully evaluated using computational thermodynamics and kinetic calculations.

Introduction

Weld metal microstructure evolution in conventional C-Mn and low-alloy steel welds has been studied extensively (Refs. 1–3). This research has supported the design of welding consumables (Refs. 4, 5) for shielded metal arc welding (SMAW), submerged arc welding (SAW), gas metal arc welding (GMAW) and gas-shielded flux cored arc welding (FCAW-G). Research to date has shown it is indeed possible to obtain an as-welded microstructure with an optimum combination of strength and toughness by controlling the inclusions, weld-cooling rates and weld-metal hardenability. Moreover, the phase transformation models are also available to predict the microstructure evolution in these welds (Ref. 6). However, the results are not generally applicable to self-shielded flux cored arc welding (FCAW-S) processes (Refs. 7–12). This is due to the complexity of oxidation and nitriding reactions that occur during solidification and the solid-state phase transformations as the weld cools to room temperature.

In self-shielded flux cored arc welding (FCAW-S), there is no intentional shielding of molten steel during welding. Consequently, the molten steel is expected to absorb large concentrations of nitrogen and oxygen from the atmosphere. Nevertheless, the welding consumables typically are prepared with a high concentration of aluminum, which reacts with dissolved oxygen and nitrogen to form oxides and nitrides. This facilitates production of sound welds without porosity. However, depending on oxidation reactions (*e.g.*, $2\underline{Al} + 3\underline{O} = Al_2O_3$) and nitriding reactions (*e.g.*, $\underline{Al} + \underline{N} = AlN$), the amount of aluminum that remains in solid solution may change and control the microstructure evolution. In the first part of this collaborative research between Oak Ridge National Laboratory and Lincoln Electric, the complex inclusion formation was investigated in detail (Ref. 13). In this work, the effect of residual aluminum that remained after oxidation and nitriding reactions on subsequent solidification and solid-state transformation was considered.

KEY WORDS

Self-Shielded
Flux Cored Arc
FCAW-S
Microstructure
δ-Ferrite
Solidification
Inclusion Formation
Phase Transformation

Experimental

Two FCAW-S weld metal systems that produce significantly different Al, O and N levels in the all-weld-metal region were selected for investigation: E70T-4 (high-aluminum welding consumable) and E71T-8 (low-aluminum welding consumable) (Ref. 14). These electrodes represent the extremes of the typical aluminum range for FCAW-S deposits in this research. Welding parameters are summarized in Table 1. The two welds were made with significantly different welding heat inputs, which were necessitated by the respective electrode diameters and were representative of actual usage. Transverse macrosections were taken from each weld. Bulk weld metal chemical compositions were determined using a BAIRD Model DV 4 omission spectrometer and LECO analysis equipment. Samples for carbon, sulfur and aluminum analyses were taken by collecting chips after drilling at the same locations. Total aluminum content was determined by atomic absorption spectroscopy following dissolution in aqua regia/hydrogen fluoride and fuming in perchloric acid. The final compositions of the welds are given in Table 2.

Thermodynamic Calculations

In this paper, interest is in solidification and subsequent solid-state transfor-

S. S. BABU and S. A. DAVID are with Oak Ridge National Laboratory, Oak Ridge, Tenn. M. A. QUINTANA is with The Lincoln Electric Co., Cleveland, Ohio.

Table 1 — Welding Conditions

	High-Aluminum E70T-4	Low-Aluminum E71T-8
Electrode diameter [in. (mm)]	0.120 (3)	0.078 (2.0)
Tip-to-work distance [in. (mm)]	2.75 (70)	0.75 (19)
Voltage	31–36	19–20
Amperage	525–590	270–280
Wire feed rate [in./min (mm/s)]	225–250 (95–106)	120 (51)
Heat input [kJ/in. (kJ/mm)]	86–98 (3.4–3.8)	54–58 (2.1–2.3)

Table 2 — Weld Metal Compositions

Weld	C	Mn	Si	Al	Ni	Ti	O	N
E70T-4	0.234	0.50	0.28	1.70	0.02	0.003	0.006	0.064
E71T-8	0.149	0.64	0.30	0.53	0.01	0.058	0.030	0.033

mation. Therefore, equilibrium calculations were limited to liquid steel, austenite, ferrite (both δ-ferrite and α-ferrite) and cementite. These calculations essentially consider the Gibbs free energy of various phases as a function of temperature and composition. The phase equilibria between these phases are calculated by using the minimization of free energy. This is schematically illustrated in Fig. 1 for Fe-Al binary system. The diagram shows a schematic variation of the free-energy composition diagram at a temperature for the equilibrium between δ-ferrite and austenite. Computational methods and thermodynamic data can be used to extend such calculations to multicomponent systems with multiple phases. The calculations in this work were performed using commercial software (ThermoCalc™ software version L) (Ref. 15). The calculations considered the elements Fe, C, Mn and Al. The effects of other minor elements were not considered because they do not lead to gross changes in phase stability. It is important to note that nitrogen has a large effect on the phase stability, even in small concentrations. However, previous work showed most of the nitrogen will be removed from the liquid as nitrides (Ref. 13). Further details on thermodynamic calculations can be found in Ref. 16.

Kinetic Calculations

Thermodynamic calculations consider only the phase stability of various phases as a function of temperature and composition. However, they do not describe the effect of weld cooling and subsequent reaction kinetics. Therefore,

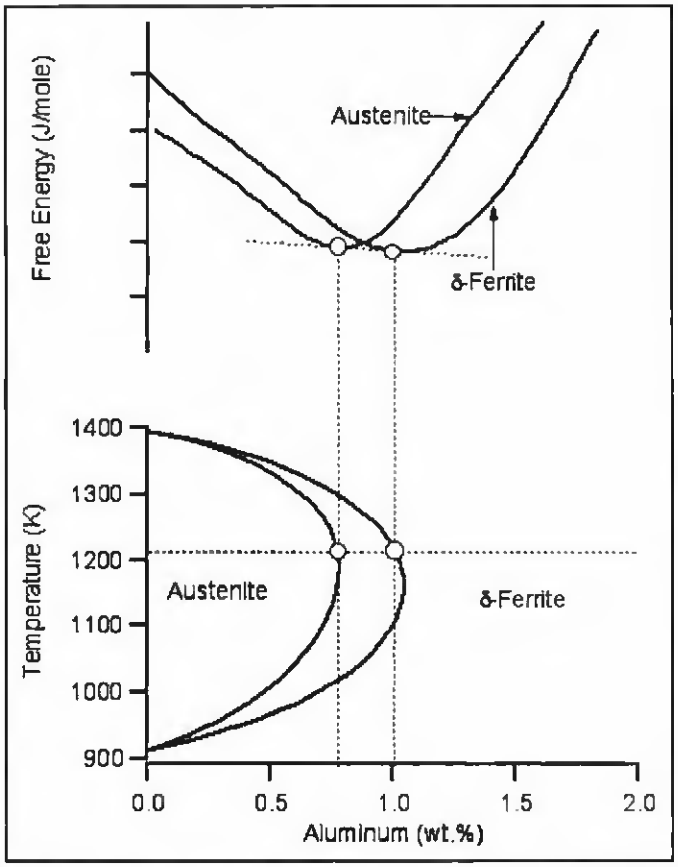

Fig. 1 — Schematic illustration of phase equilibria between δ-ferrite and austenite in Fe-Al system at a given temperature.

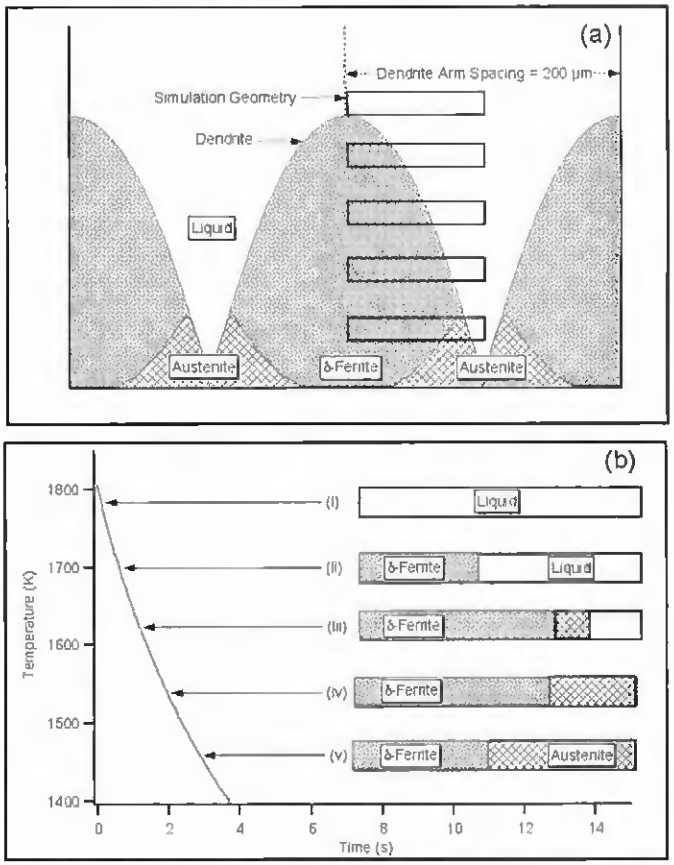

Fig. 2 — A — Schematic geometry used in the diffusion-controlled solidification simulations; B — schematic illustration of various stages of microstructural evolution modeled by the diffusion-controlled growth calculations.

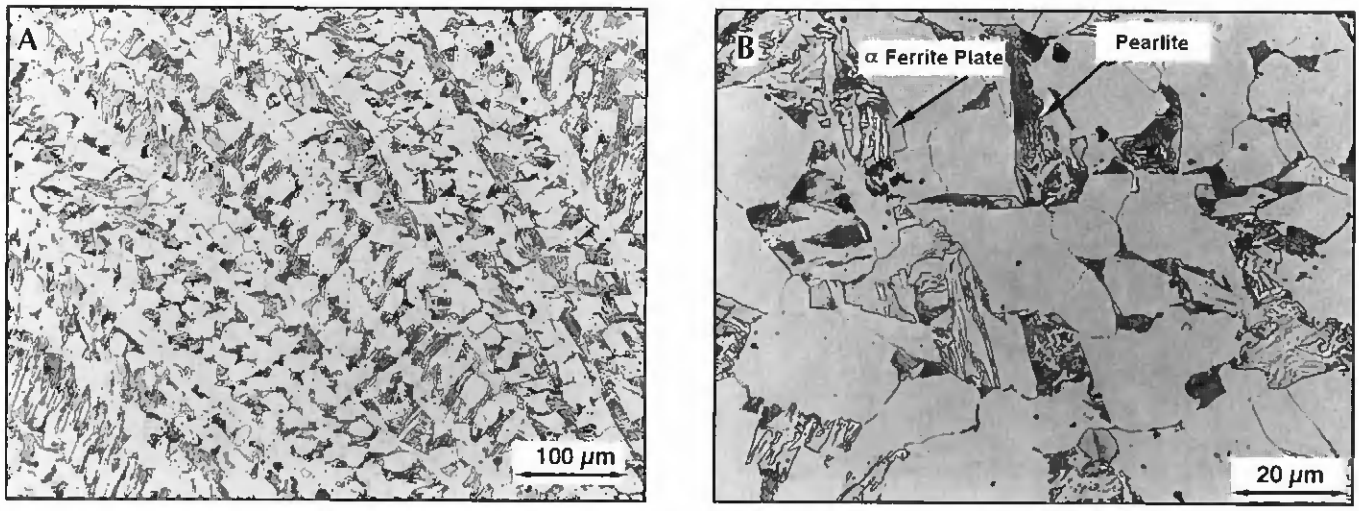

Fig. 3 — A — Micrograph from the unrefined region of the high-aluminum weld showing the skeletal δ-ferrite microstructure; B — a high-magnification micrograph showing the α-ferrite plates and pearlite (marked by arrows) that formed from the austenite.

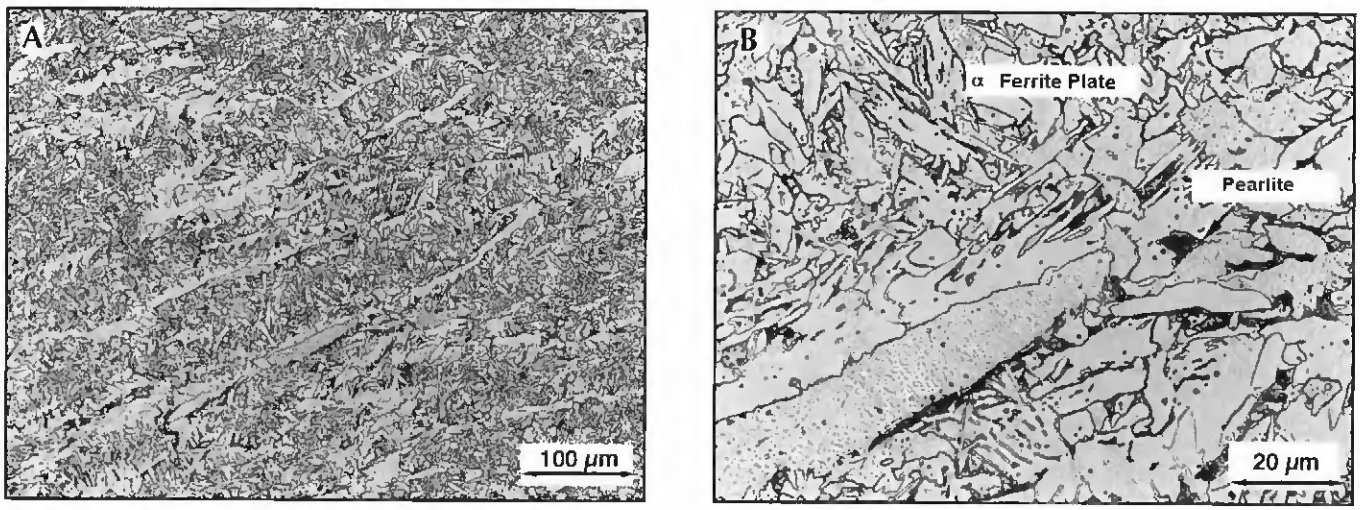

Fig. 4 — A — Micrograph from the unrefined region of the low-aluminum weld showing classic α-ferrite microstructure; B — high-magnification micrograph showing the higher fraction of low-temperature α-ferrite plates and pearlite (marked by arrows) that formed from the austenite.

one-dimensional, diffusion-controlled solidification calculations were performed to evaluate the solidification and subsequent diffusion-controlled growth of austenite and δ-ferrite after solidification. It is important to note we need not consider the nucleation of solids in these calculations because the solidification continues epitaxially from the heat-affected zone. The calculations ignore the effect of dendrite tip undercooling due to uncertainty in estimating them for these unique steel compositions under weld-cooling conditions. The calculations assume local equilibrium at the interface between phases and consider diffusion in liquid and solid phases. In addition, a constant dendrite arm spacing of 200 μm was assumed for the calculations. The calculations were performed using DicTra software (Refs. 17, 18) and standard solid solution and mobility databases (Refs. 15, 18).

The schematic illustration of the geometry used for diffusion-controlled growth calculations is shown in Fig. 2. This geometry considers a small volume element, as shown in Fig. 2A. Various stages of microstructure evolution considered in this calculation are shown in Fig. 2B.

At the start of solidification, the calculation considers the growth of both ferrite and austenite phases into liquid steel. One of the phases is chosen based on thermodynamic feasibility.

In the welds under consideration, the δ-ferrite is expected to form first and grow into the liquid. With further cooling, δ-ferrite grows and partitions alloying elements into the liquid. The calculations monitor this partitioning and allow for the formation of austenite at the liquid/δ-ferrite interface based on comparative thermodynamic feasibility.

At a critical temperature, the austenite will start growing into both liquid and δ-ferrite. This condition is similar to a peritectic reaction that is expected in these steels.

With further cooling, the liquid steel will be consumed by this austenite growth. It is important to note that, at these conditions, the calculations are tracking the movement of both δ-ferrite-austenite and liquid-austenite interfaces based on diffusion in liquid, austenite, and δ-ferrite.

At the end of solidification, the calculations are continued further to consider the equilibration between the austenite and δ-ferrite. Calculations were stopped as soon as the temperature reached ~1600 K. The calculations allow for the prediction of the amount of residual δ-ferrite that may remain at room tem-

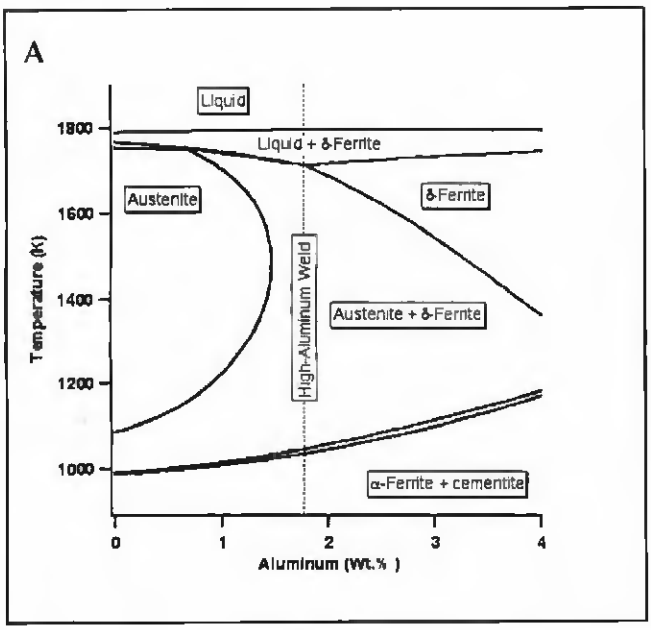

Fig. 5 — A — Quasi-binary Fe-Al diagram for the high-aluminum weld (the dotted line represents the actual bulk aluminum concentration) considering Fe, Al, Mn and C interactions; B — equilibrium phase fractions of ferrite and austenite as functions of temperature for the same weld metal.

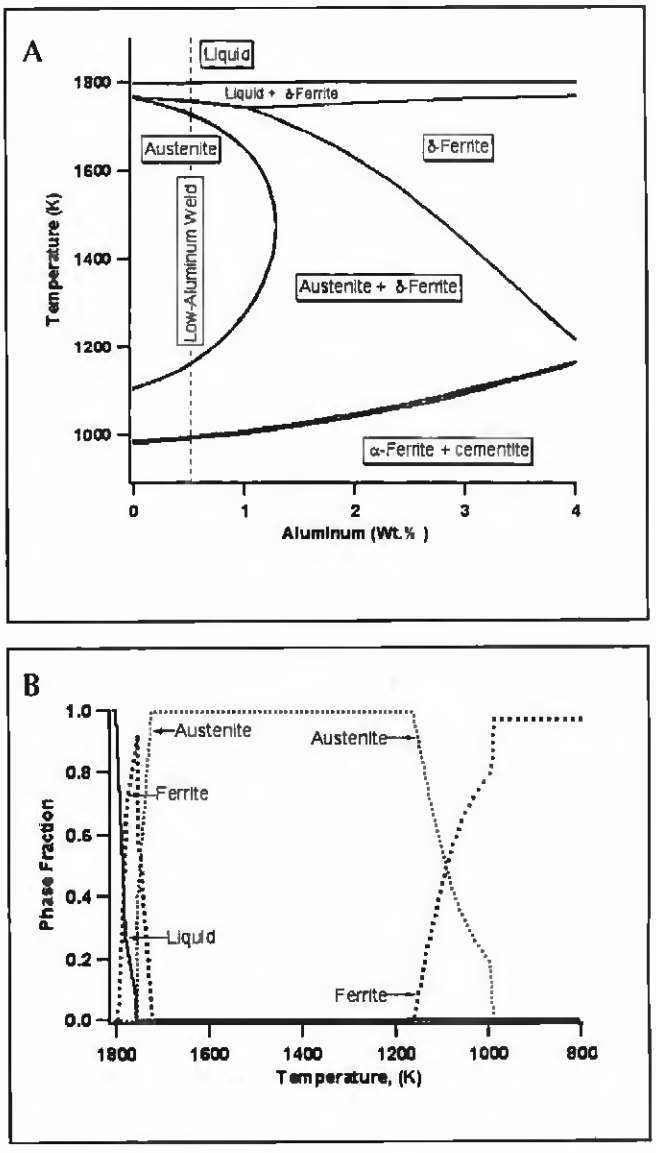

Fig. 6 — A — Quasi-binary Fe-Al diagram for the low-aluminum weld (the dotted line represents the actual bulk aluminum concentration); B — equilibrium phase fractions of ferrite and austenite as functions of temperature for the same weld metal.

perature. The calculations were performed for both the welds given in Table 2 and for two different linear weld cooling rates of 1 and 10 Ks^{-1}.

Results

Weld Metal Microstructure

The as-welded microstructure of a high-aluminum weld is shown in Fig. 3. The microstructure shows classic skeletal δ-ferrite grains — Fig. 3A. This is in agreement with previous research (Refs. 7–12). High-magnification micrographs (Fig. 3B) also show there are small islands containing α-ferrite plates and pearlitic microstructure. This suggests that, in these welds, some amount of austenite (30–40%) should be present after solidification at elevated temperature. This austenite decomposes to Widmanstätten ferrite plates and also pearlitic structure during further cooling.

In contrast, the low-aluminum weld showed no indication of skeletal δ-ferrite morphology hut instead exhibited classic columnar grains delineated by α-ferrite structure — Fig. 4. Original austenite columnar grains were transformed into grain-boundary α-ferrite structure, Widmanstätten ferrite and a small amount of pearlite. This suggests that the low-aluminum weld should be 100% austenite at high temperature. One can also observe the microstructure obtained with low-aluminum welds, which is fine, and therefore, may exhibit better mechanical properties (Ref. 13). Such a large change in microstructure with differences in aluminum and carbon concentration is intriguing (Table 2).

Phase Equilibria

The results from phase equilibrium calculations are presented in Figs. 5 and 6. The quasi-binary Fe-Al diagram (Fig. 5A) shows an overview of phase stability for the high aluminum weld metal. It is important to note these calculations consider the effects of C and Mn also. The phase diagram for a high-aluminum weld indicates that, as the weld cools, the liq-

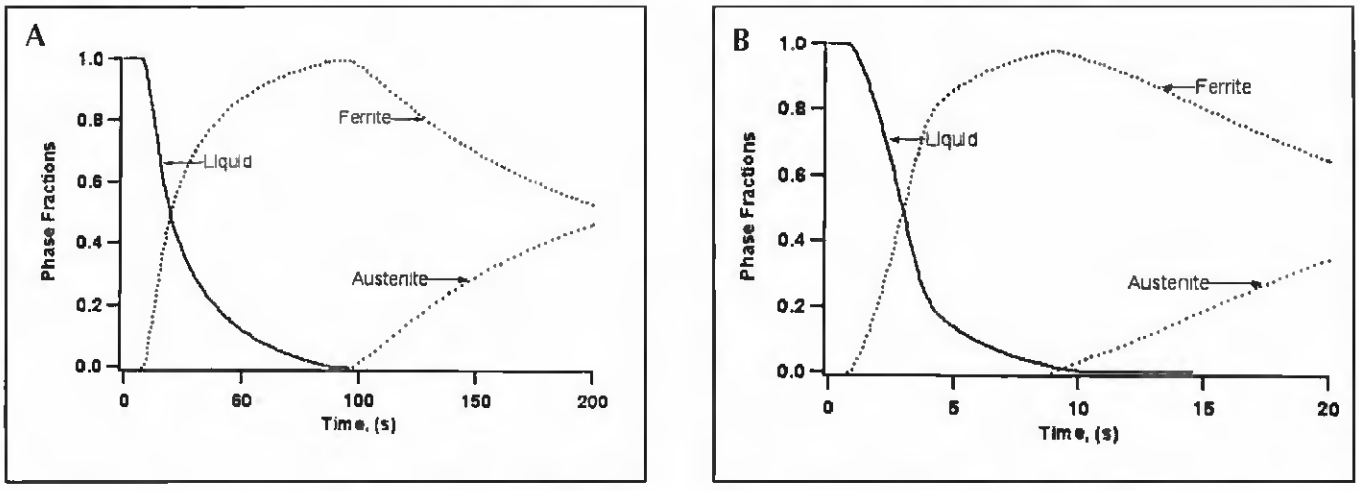

Fig. 7 — Predicted phase fractions in the high-aluminum weld as a function of time. A — 1 Ks^{-1}; B — 10 Ks^{-1}.

uid will first solidify as δ-ferrite. On further cooling, the alloy will enter two-phase ferrite + austenite region. Subsequent cooling will allow for equilibration between ferrite and austenite over a large temperature range (1709 to 1043 K).[1] As cooling continues below ~1000 K, the weld is expected to decompose into a mixture of ferrite and cementite. The above sequences can also be summarized in the form of phase fraction for this weld in Fig. 5B. An interesting observation is the reversal of austenite stability below and above 1400 K. These calculations clearly show a high-aluminum weld will not yield 100% austenite at high temperature, and are in qualitative agreement with the experimental microstructure, which shows the presence of skeletal δ-ferrite.

In contrast, the calculations for the low-aluminum welds (Fig. 6) show a different behavior. The summary of calculations (Fig. 6B) indicates the liquid will solidify as δ-ferrite first as the weld cools. Continued cooling of this weld will induce austenite formation from the liquid. Immediately after the solidification, there is a temperature range over which the δ-ferrite and austenite may coexist; however, on cooling below 1728 K, the whole weld is expected to form 100% austenite. On further cooling to 1165 K, the α-ferrite is expected to grow at the expense of austenite and to transform completely into ferrite and small amounts of cementite. The above results are also in qualitative agreement with the experimental microstructure, which shows only the presence of classical α-ferrite microstructure.

1 Relation between K and °F: °F = [K x (9/5)] – 460.

Diffusion-Controlled Growth Kinetics

Thermodynamic calculations described the observed microstructure evolution successfully. However, there is a need to describe these microstructure evolutions as functions of weld cooling rates. This is needed to evaluate the sensitivity of microstructural constituents to a wide range of welding-process parameters. In this regard, thermodynamic calculations do not yield any insight. Therefore, the microstructure evolutions in these two welds were simulated for linear cooling rates of 1 and 10 Ks^{-1} by using the methodology described earlier.

The calculated phase fractions in the high-aluminum welds as functions of time for both cooling rates are shown in Fig. 7. For both cooling rates, the primary solidification was as δ-ferrite. Moreover, toward the final stages of solidification, the austenite was found to nucleate at the liquid/δ-ferrite interfaces and to grow into both the δ-ferrite and the liquid. The only difference between the two different cooling rates was the fraction of the residual δ-ferrite that remains stable at 1600 K. At 1 Ks^{-1}, the ferrite content (53%) was lower than that calculated for 10 Ks^{-1} (65%). Therefore, results indicate that, as the cooling rate increases, a large amount of δ-ferrite will be retained in the weld at room temperature. This result can be further clarified by comparing the δ-ferrite fraction predicted from these calculations and equilibrium calculations, as shown in Fig. 8. The results show the deviation from the equilibrium ferrite fraction will be more as the cooling rate increases. The δ-ferrite fraction in the high-aluminum weld (Fig. 3) was measured to be 0.596. During this measurement, care was taken to exclude the transformation products from the austenite in-between the δ-ferrite grains. The measured δ-ferrite fraction value is in agreement with the predicted values in Fig. 8. It will be of interest to evaluate the δ-ferrite fraction at different cooling rate conditions by employing low-heat-input welds.

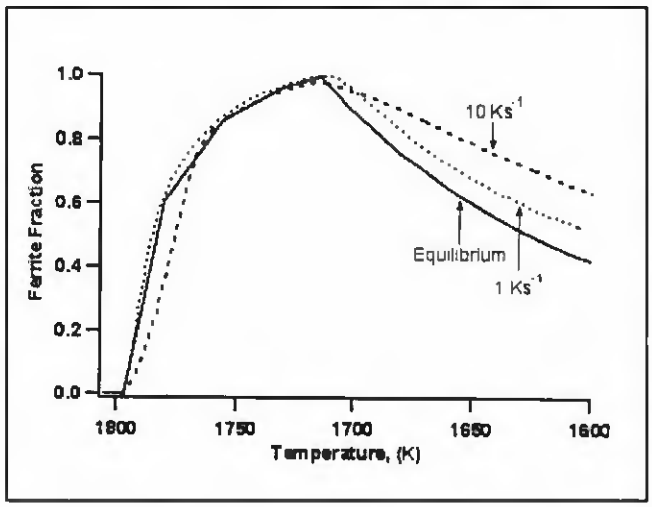

Fig. 8 — Comparison of predicted ferrite fraction in the high-aluminum weld for equilibrium and different cooling rates.

The calculations for the low-aluminum welds showed the alloy would solidify as δ-ferrite for both cooling rates

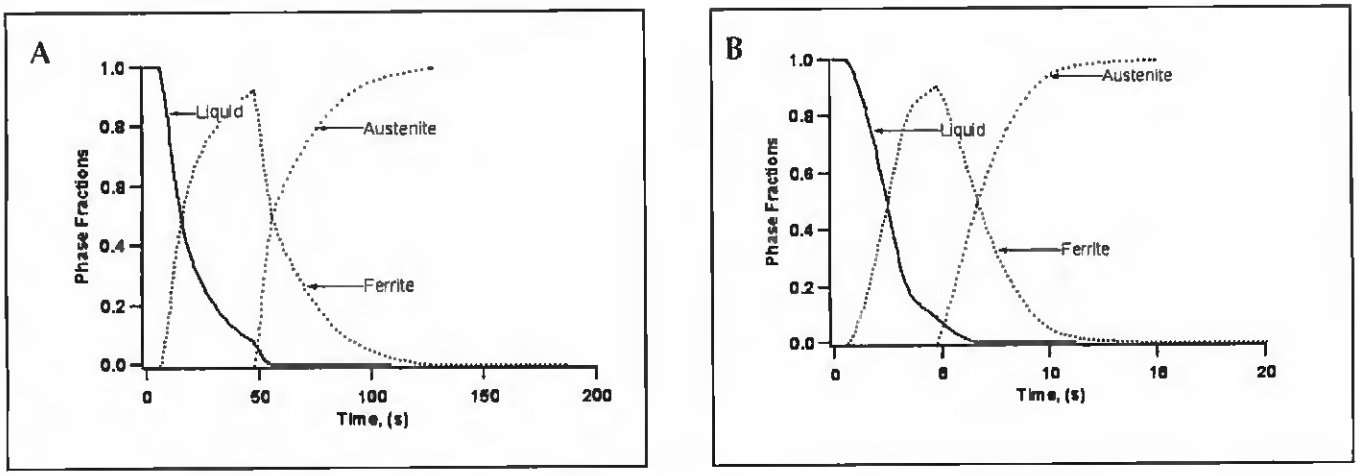

Fig. 9 — Predicted phase fractions in the low-aluminum weld as a function of time. A — 1 Ks^{-1}; B — 10 Ks^{-1}.

— Fig. 9. After some fraction of δ-ferrite formation, the austenite was calculated to nucleate at the liquid/δ-ferrite interface and to grow into both δ-ferrite and liquid. However, in contrast to a high-aluminum weld, the weld is expected to form 100% austenite for both cooling rates. The only difference was found to be the time required for the austenite content to reach 100%.

Discussion

The present results have an immense impact on the optimization of weld metal systems. Assuming the design of a welding process involves the selection of weld metal composition and process parameter ranges to obtain a particular desired microstructure and properties, such predictive calculations could be instrumental. Further, they offer an alternative to the traditional trial-and-error method of producing experimental weld compositions and a process parameter matrix and evaluating these welds by microstructural observations, tensile testing and impact testing (Ref. 2). This method, however, is time-consuming and expensive.

An alternative methodology would be to use computational methods to evaluate the microstructure development over a wide range of compositions and process parameters. After these calculations are performed, a narrow weld-metal composition matrix and process parameter range can be tested experimentally for confirmation of the predictions and for standardization. The present results clearly demonstrate the potential of this alternative design methodology. In this method, there are three basic steps.

1) *Control of oxide and nitride formation.* In the first step, thermodynamic and kinetic calculations can be used to describe the oxide and nitride reactions in the weld metal. This has been a topic of study in earlier work by the authors and other researchers (Refs. 19–22). For example, in a previous paper by the authors, the inclusion formation that takes place during the FCAW-S process was described (Ref. 13). This work showed that the nitriding conditions lead to larger residual aluminum in the weld metal compared to the oxidizing conditions. This phenomenon was attributed to the thermodynamic interactions of dissolved aluminum, nitrogen and oxygen in the weld metal. In situations where continued addition of aluminum does not lead to any oxidation reactions, these interactions essentially produce more AlN precipitates. However, if aluminum concentration is reduced, one can promote the oxidation reactions and thus reduce the residual aluminum in the liquid steel. This control is not simple, and one needs to perform detailed thermodynamic and kinetic analysis to steer the oxidation, or nitriding reactions, in the weld pool.

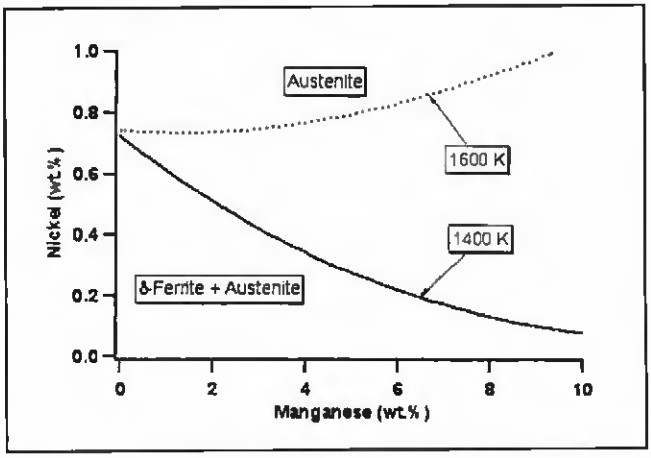

Fig. 10 — Calculated phase boundary between two-phase (δ-ferrite and austenite) and single-phase austenite regions at 1400 K and 1600 K with a base composition of the high-aluminum weld.

2) *Weld composition control.* In this step, thermodynamic calculations can be used to establish the baseline weld metal composition qualitatively. Boundary limits can be designed to influence a particular microstructore evolution. The results given in Figs. 5 and 6 are examples of this step. Immediately, it is noticeable that the selection of weld metal composition in this manner is not an independent step; rather, it depends on step 1. Nevertheless, one can modify other alloying elements that may not directly take part in the oxidation or nitriding reactions in the liquid steel. In the present case, the candidate alloying additions might be Ni, Mn, Cr and Si, which are protected by aluminum and do not take part in the oxidation or nitriding reactions. An example calculation was performed for a high-aluminum weld at 1400 K to show the phase fields as functions of Ni and Mn addition — Fig. 10. This calculation shows one could promote the austenite stability more efficiently by adding nickel than by adding manganese. This weld metal composition also significantly affects the weld microstructure and the properties of welds made with mixed processes (*i.e.*, SMAW and FCAW-S) (Ref. 23). These mixed-process techniques will yield widely varying weld composition due to dilution effects.

3) *Welding process parameter control.* In this step, the kinetic calculations can be used to set parameter boundary limits for the welding process so that one can achieve the required microstructure within those limits for a given weld-metal composition. The results given in Figs. 6–8 are the examples of this step. This will be a crucial parameter if a particular weld-metal composition is very close to the austenite and austenite + δ-ferrite phase boundary. For example, if the aluminum concentration was reduced to 1.4 wt-% in the high-aluminum weld, it is indeed possible to reach 100% austenite over a temperature range of 1414 to 1551 K — Fig. 5. However, the formation of 100% austenite will depend on how fast the weld metal cools. If the cooling rates are fast, then there will not be sufficient time for δ-ferrite to transform completely to austenite and residual skeletal δ-ferrite morphology may be observed. Therefore, to obtain a 100% austenite weld, under the given conditions, the lower limit of the weld heat input (or the highest cooling rate) must be maintained in the weld metal region. It is important to note that, in the present calculations, the weld cooling rates considered are typical of those experienced by FCAW-S processes. Further work is necessary to extend this work to very low heat input conditions.

Conclusions

Weld metal microstructures were investigated in commercial FCAW-S steel welds with two different aluminum concentrations. The weld with high aluminum concentration exhibited a skeletal columnar δ-ferrite microstructure. The weld with low aluminum concentrations exhibited classic α-ferrite plates and pearlite microstructure.

Thermodynamic calculations suggested this microstructure development would be related to phase stability of liquid, δ-ferrite and austenite. The calculations indicated the primary solidification mode will be ferrite and that austenite will form during subsequent cooling in both welds. In the high-aluminum weld, the transformation from δ-ferrite to austenite was found to be incomplete due to the higher stability of δ-ferrite. This led to a skeletal columnar δ-ferrite morphology reminiscent of δ-ferrite columnar dendrites formed during weld solidification. In contrast, for the low-aluminum weld, the calculations showed the δ-ferrite transforms completely to austenite at high temperature and then decomposes to a low-temperature α-ferrite morphology during further weld cooling.

The effect of the weld-cooling rate (1 and 10 Ks^{-1}) on weld solidification and on the growth of austenite and δ-ferrite was simulated using diffusion-controlled growth calculations. The results showed that, in high aluminum welds, the weld cooling rate affects only the fraction of residual δ-ferrite, which was found to be more with 10 Ks^{-1} than that of 1 Ks^{-1}. Welds with low-aluminum concentrations showed complete transformation to austenite from δ-ferrite on weld cooling for both cooling rates.

The results demonstrated that it is indeed possible to use computational thermodynamic and kinetic modeling tools to design welding consumables.

Acknowledgments

Research sponsored by the Division of Materials Science and Engineering, U.S. Department of Energy, and Assistant Secretary for Energy Efficiency and Renewable Energy, Office of Industrial Technologies, Metals Processing Laboratory User Center (MPLUS), Advanced Industrial Materials Program under contract DE-AC05-00OR22725 with UT-Battelle, LLC.

References

1. Abson, D. J., and Pargeter, R. J. 1986. Factors affecting as-deposited strength, microstructure, and toughness of manual metal arc welds suitable to C-Mn steel fabrications. *Int. Met. Reviews* 31: 141.

2. Evans, G. M., and Bailey, N. 1986. *Metallurgy of Basic Weld Metal.* Abington Publishing, Cambridge, England.

3. Grong, O., and Matlock, D. K. 1986. Microstructural development in mild and low alloy steel weld metals. *International Metals Review* 31: 27–48.

4. Liu, S., and Olson, D. L 1986. The role of inclusions in controlling HSLA weld microstructures. *Welding Journal* 65(6): 139-s to 149-s.

5. Fleck, N. A., Grong, O., Edwards, G. R., and Matlock, D. K. 1986. The role of filler metal wire and flux composition in submerged arc weld metal transformation kinetics. *Welding Journal* 65(5): 113-s to 121-s.

6. Bhadeshia, H. K. D. H., Svensson, L.-E., and Gretoft, B. 1985. A model for the development of microstructure in low-alloy steel (Fe-Mn-Si-C) weld deposits. *Acta Metallurgica* 33: 1271–1283.

7. Krivenko, L. F. 1967. Research into the nitrides in the weld metal when steel is welded by open arc process. *Avto. Svarka* 7: 6–9.

8. Dorling, D. V., Rodriguez, P. E. L. B, and Rogerson, J. H. 1976. A comparison of the toughness of self-shielded arc and submerged arc weld metals in C-Mn-Nb steels, part 1: effect of consumables and process variables on weld metal toughness. *Welding and Metal Fabrication* 7/8: 419–423.

9. Dorling, D. V., Rodriguez, P. E. L. B., and Rogerson, J. H. 1976. A comparison of the toughness of self-shielded arc and submerged arc weld metals in C-Mn-Nb steels, part 2: through thickness toughness variation. *Welding and Metal Fabrication* 9: 479–481.

10. Kotecki, D. J., and Moll, R. A. 1970. A toughness study of steel weld metal from self-shielded flux cored electrodes — part I. *Welding Journal* 49(4): 157-s to 165-s.

11. Kotecki, D. J., and Moll, R. A. 1972. A toughness study of steel weld metal from self-shielded flux cored electrodes — part II. *Welding Journal* 51(4): 13B-s to 155-s.

12. Es-Souni, M., Beaven, P. A., and Evans, G. M. 1992. Microstructure and AEM studies of self-shielded flux cored arc weldments. *Welding Journal* 71(2): 35-s to 45-s.

13. Quintana, M., McLane, J., Babu, S. S., and David, S. A. 2001. Inclusion formation in self-shielded flux cored arc welds. *Welding Journal* 80(4):98-s to 105-s.

14. American Welding Society. 1995. AWS A5.20, *Specification for Carbon Steel Electrodes for Flux Cored Arc Welding.*

15. Sundman, B., Jansson, B., and Andersson, J. O. 1985. The thermo-calc databank system. *Calphad* 9:1–153.

16. Hsieh, K. C., Babu, S. S., Vitek, J. M., and David, S. A. 1996. Calculation of inclusion formation in low alloy steel welds. *Materials Science and Engineering,* A215, 84–91.

17. Andersson, J-O, Höglund, L., Jönsson B., and Agren, J. 1990. *Fundamentals and Applications of Ternary Diffusion,* ed., G. R. Purdy. New York, Pergamon Press, pp. 153–163.

18. Engström, A., Höglund, L., and Agren, J. 1994. Computer simulation of diffusion in multiphase systems. *Metall. Mater. Trans.* A. 25A, 1127–1134.

19. Kluken, A. O., and Grong, O. 1989. Mechanisms of inclusion formation in Al-Ti-Si-Mn deoxidized steel weld metals. *Metallurgical Transactions* 20: 1335–1349.

20. Onsoien, M. I., Liu, S., and Olson, D. L. 1996. Shielding gas oxygen equivalent in weld metal microstructure optimization. *Welding Journal* 75(7): 216-s to 224-s.

21. Babu, S. S., David, S. A., Vitek, J. M., Mundra, K., and DebRoy, T. 1995. Development of macro- and microstructures of C-Mn low alloy steel welds — inclusion formation. *Materials Science and Technology* 11:186–199.

22. Babu, S. S., Reidenbach, F., David, S. A., Böllinghaus, Th., and Hoffmeister, H. 1999. Effect of high energy density welding process on inclusion and Microstructure formation in steel welds. *Science and Technology of Welding and Joining* 4: 63–73.

23. Johnson, M., and Quintana, M. 1999. Micromechanisms of fracture in structural steel and high-strength steel multipass weld metals. Presented at the 80th American Welding Society Annual Meeting, April 12–15, 1999.